Corrugation Reinforced Architectured Materials by Direct Laser Hardening: A Study of Geometrically Induced Work Hardening in Steel

Zhige Wang, Olivier Bouaziz, Justin Dirrenberger, and Pierre Lapouge*

Improving the strength-to-ductility trade-off remains the prime driving force for the development of advanced high-strength steel. Traditionally research breakthroughs are focused on the microstructure and relative phase composition. Herein, laser hardening is applied to ductile ferritic steel to introduce straight and corrugated martensitic reinforcements, effectively generating architectured steel sheets. Tensile behavior of laser-architectured samples is studied both using finite-element method simulation and mechanical testing to reveal the effect of laser-induced corrugations on strength and necking strain. The results show that with the same reinforced volume fraction of 24%, an increase in corrugation height/period leads to a gain in necking strain with a loss in yield strength and ultimate tensile stress. This beneficial effect on necking strain is due to the corrugation unbending process which introduces so-called geometric work hardening during tension. Extended simulations are carried out on various corrugation heights/periods and the evolution trends of ultimate tensile strength and necking change with different reinforced volumes. This study proposes a perspective on corrugation-reinforced architectured materials. Corrugation parameters can be chosen to tailor the mechanical behavior of laser-architectured materials.

1. Introduction

Inheriting from composite and hybrid materials, architectured materials are a rising class of materials that bring new possibilities in terms of functional properties, filling the gaps, and pushing the limits of Ashby's materials performance maps.[1,2] Architectured materials refer to heterogeneous materials in which the topology of different phases is engineered in order to yield structural effects.[3] By designing shape and scale of the architecture, architectured materials may exhibit optimized properties surpassing the arithmetic average of their constituents.[1] Synergistic effect can be obtained from the interaction and coupling between heterogeneous zones, for example, the strength-to-ductility tradeoff.[4] Some limitations can be overcome and desired combinations can be achieved, filling gaps in the material–property space representing existing monolithic and composite materials.[1,5,6] Different kinds of architectured materials are being developed in various manners for different objectives, such as lattices,[7–13] auxetics,[14–20] interlocks,[21–25] compositionally graded materials,[26–29] and many others.

Different studies can be found in the literature regarding the fabrication of metallic architectured materials, especially in Fe–C system, because the effect of carbon atoms plays a key role to the phase constitution and mechanical properties. A filamentary microscale duplex stainless steel has been developed by accumulative drawing and rebundling technique, which offers a possibility to multiphase composites beyond thermodynamic equilibrium conditions.[30] Local carburization and decarburization by controlling atmosphere and protecting masks have been proposed to create a hierarchical architecture of ferrite and martensite to overcome the contradiction between ductility and strength.[28,29] Azizi et al.[31] observed an equivalent strain over 2.0 by forming local shear bands in surface-decarburized martensitic steel. Their following studies show that this method can be combined with intercritical heat treatments to control the grain size at the shear bands and produce strengthened heterogenous dual-phase steels with gradient in both carbon content and grain size.[32,33]

In metallurgical research, a high strain hardening of materials is often expected to mitigate plastic strain localization.[34] Studies aiming at increasing the strain hardening are mostly focused on

Z. Wang, J. Dirrenberger, P. Lapouge
PIMM, Arts et Metiers, CNRS, Cnam
HESAM Université
75013 Paris, France
E-mail: justin.dirrenberger@ensam.eu

O. Bouaziz
Laboratoire d'Etude des Microstructures et de Mécanique des Matériaux (LEM3)
CNRS
Université de Lorraine, Arts et Métiers
57000 Metz, France

O. Bouaziz
Laboratoire d'Excellence DAMAS
CS 50840, 54011 Nancy Cedex, France

The ORCID identification number(s) for the author(s) of this article can be found under https://doi.org/10.1002/srin.202200695.

microstructural aspects, such as grain refining and phase repartition[35,36] and twinning-induced plasticity.[37] Bouaziz[5] proposed the concept of geometrically induced strain hardening using corrugated reinforcements embedded in a matrix, whose unbending process during uniaxial loading delays the overall strain hardening decrease.

Several studies have brought results regarding the mechanical behavior of corrugated materials. Thill et al.[38] and Dayyani et al.[39] studied the tensile behavior of the isolated corrugated core of different fiber/epoxy composites and found that strain hardening decreased in the beginning, followed by an increase due to the unbending process, and then decreased as classical stress–strain response. Fraser et al.[40] investigated a copper–steel system and the effect of geometric parameters of corrugated reinforcements. Bouaziz[5] simulated the tensile test of unit cell matrix reinforced with corrugation with different yield stresses and perfect plastic behavior. These studies have shown the interest of corrugation compared to straight reinforcement, in terms of strain hardening and delayed necking.

Bouaziz[5] suggested that laser heat treatment could create reinforcements on steel materials by local fast quenching due to high heating and cooling rate. Ductile ferrite-based steel is heated above austenization temperature and hard martensite is formed upon rapid cooling which reinforces the matrix. The present study will adopt this idea to fabricate corrugation reinforced steel by laser heat treatment. The study of Fraser et al.[41] showed that for a given matrix, a minimum yield stress of the reinforcement was needed to achieve an enhanced necking strain and that this effect is more obvious with the increase of the yield stress.

When finely controlled, laser processing can generate deterministically graded or homogeneous topographical, mechanical, or metallurgical alterations, in surface or volume, depending on laser parameters and configuration for the treatment, thus enabling architecture through various routes.[42] Localized laser heat treatment is a promising advanced processing route for creating architectured materials.[43–46]

To the knowledge of the authors, no published work has explored the mechanical behavior of laser-architectured corrugated materials by both experimental and computational approaches. The aim of this work is to further our understanding of the mechanics of corrugated architectured materials and the beneficial effect on necking strain induced by corrugated reinforcement. To do so, microstructural and mechanical properties are characterized before and after treatment in order to identify the behaviour of so-called matrix and reinforcing phases. Sinusoidal laser treatment patterns are applied as corrugated reinforcements to be compared with straight ones, and different geometrical parameters are investigated numerically and experimentally to evaluate the effect on strain hardening. The study is extended through finite-element simulations in order to explore a larger spectrum of geometrical parameters. Different material–property maps are established as a way to select suitable corrugation patterns for given mechanical behaviour.

2. Experimental Section

The as-received material in this study was commercialized by ArcelorMittal as MS1500EZ, which was fully martensitic grade with 0.2 wt% carbon and was chosen for creating an important contrast in yield stress between the matrix and the reinforcement. It was cold rolled to form 1 mm-thick sheets and galvanized with a thin zinc layer of a few μm. The chemical composition is shown in **Table 1**. These sheets were soaked in diluted hydrochloric acid (HCl) to remove the zinc layer to avoid exposure of zinc in high temperature. After cleaning and drying, uncoated sheets were homogenized by annealing above Ac3 at 850 °C in a traditional furnace for 1 h and cooled down in the turned-off furnace to room temperature to obtain a ferritic microstructure. The oxide layer formed in the furnace was removed by HCl and the sheets were sand blasted before laser treatment to increase the absorption coefficient. Localized quenching was obtained by direct laser heat treatment.

Figure 1a shows the laser treatment platform. Two lasers were placed on each side to be used simultaneously in order to obtain a more homogeneous microstructure through the whole thickness of the sheets. The two lasers available for this study were a single-mode 500 W fiber laser from SPI (Southampton, UK) treating surface A at a wavelength of 1080 nm with a focal distance of 199 mm and a multimode 110 W laser diode from DILAS (Mainz, Germany) for surface B at a wavelength of 980 nm with a 200 mm focal distance. They were used simultaneously in order to achieve a more homogeneous hardened zone in the steel sheet thickness. The steel sheets were fixed in an aluminum alloy frame to avoid thermal deformation during the treatment. The frame was fastened on a 6-axis Kuka Agilus KR6 R900 robotic arm which could move with preprogrammed trajectories for various reinforcement patterns. Argon was used as shielding gas to avoid oxide formation on the sheet surfaces at high temperature. The input power was set at 150 W for surface A with fiber laser and 100 W for surface B with diode laser, and the robot moving velocity was 10 mm s^{-1}. These settings were determined based on previous work[44] and parametric optimization for this specific material.

Figure 1b,c shows the schematic images of a sample with straight reinforcement and a corrugation reinforced sample at the gauge parts. The spot size of straight reinforcement was set at 1.2 mm, which resulted in a 24% volume fraction sample to be laser treated. The sinusoidal patterns presented three key parameters: period (P), height (H), and thickness (t), among which P and H defined the corrugation shape, while t depended on the spot size. For the corrugated reinforcement, the spot size was slightly adjusted by defocusing the lasers, to keep the same laser-treated volume fraction in the gauge area. **Table 2** shows the chosen geometric parameters in this study. Figure 1d shows the samples with chosen geometric parameters in Table 2.

Microstructural observations were performed on cross section of annealed steel and also after laser quenching treatment using a Zeiss Axio optical microscope and Zeiss EVO MA-10 scanning electron microscope (SEM) equipped with a Nordif UF1000 (Trondheim, Norway) electron backscatter diffraction detector (EBSD). Prior to the observations, the samples were prepared by grinding with silicon carbide abrasive papers with grit sizes

Table 1. Chemical composition (wt%) of as-received MS1500EZ.

C	Mn	Si	Cr	Fe
0.228	1.730	0.242	0.190	Bal.

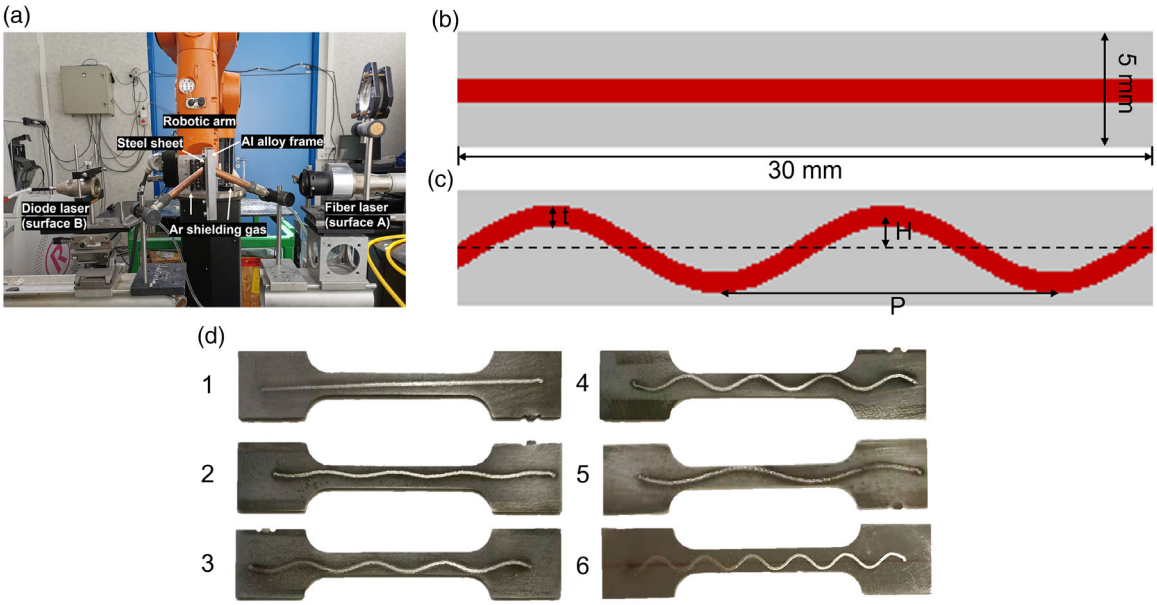

Figure 1. a) Laser treatment platform, b) sample with straight reinforcement, c) sample with corrugated reinforcement, and d) experimental samples 1–6.

Table 2. Geometrical parameters of reinforcements for the samples considered in this study.

Sample	Period P [mm]	Height H [mm]	Inclination [H/P]	Thickness t [mm]
1	∞	0	0	1.20
2	15	0.5	0.033	1.19
3	15	1.0	0.067	1.15
4	15	1.5	0.1	1.10
5	30	1.5	0.05	1.16
6	10	1.5	0.15	1.01

of 240, 400, 800, 1000, followed by cloth polishing using 9, 3, and 1 μm diamond suspension solutions. Then they were etched in 3% nital solution for a few seconds to reveal the microstructure. Samples submitted to EBSD analysis were finished by 0.04 μm colloidal silica suspension (OP-S) for 30 min after polishing. Vickers microhardness tests were carried out using a Matsuzawa MMT-X7A (Akita, Japan) on the cross section of annealed and laser-quenched materials with a force of 200 gf and a load time of 10 s to estimate the mechanical property changes due to heat treatment.

Laser architectured samples were submitted to uniaxial tensile tests on a Instron 5581 at the speed of 1 mm min^{-1}, coupled with digital image correlation (DIC) displacement field measurement to follow the local strain evolution of matrix and reinforcement with the VIC-2D software from Correlated Solutions (Irmo, SC, USA). At least 4 specimens were tested for each configuration. Numerical and experimental results were compared to evaluate the geometry-induced work hardening and the enhancement in necking strain due to corrugated reinforcements.

Behavior of architectured steel with straight and corrugated reinforcement during tensile test was predicted by finite-element analysis using ABAQUS. An example of ABAQUS simulation of tensile test model with a corrugated reinforcement is shown in **Figure 2**. One side was fixed with ENCASTRE boundary condition, and a uniform displacement was imposed at the other side. The mesh size was around 0.3 mm at the gauge length and a max step size of 0.002 was applied.

3. Results

3.1. Mechanical and Microstructural Characterization of the Matrix and Reinforcement

Figure 3a shows a micrography of the laser-hardened zone section, which consists of a fully martensitic zone, a transition zone, and ferritic annealed material. In the fully martensitic zone, a small fusion zone is formed on the upper side due to the high energy density of the fiber laser. Microhardness along the section center line (track 1 on Figure 3a) is shown in Figure 3b. The average microhardness in the fully martensitic zone is 420 Hv compared to 174 Hv of the annealed material. Between these two zones is the transition region, where decreasing martensite percentage results in reduced hardness. Figure 3c shows the microhardness along the beam center marked as track 2 in Figure 3a. Besides the smaller values (380 Hv) near both surfaces due to decarburization during the annealing process in the furnace, the hardness is rather stable through the thickness (440 Hv).

Figure 4a shows the EBSD image quality (IQ) map of the annealed material, transition region, and martensitic zone from top to bottom, with ferrite and pearlite grains being light with high IQ and martensite being dark with low IQ. The annealed material contains mostly ferrite and embedded pearlite where the excess carbon atoms are rejected during the equilibrium cooling in the furnace (cf. Figure 4b). In the transition zone, pearlite transforms into austenite when heated above Ac1 and martensite is formed upon cooling, but due to the insufficient temperature

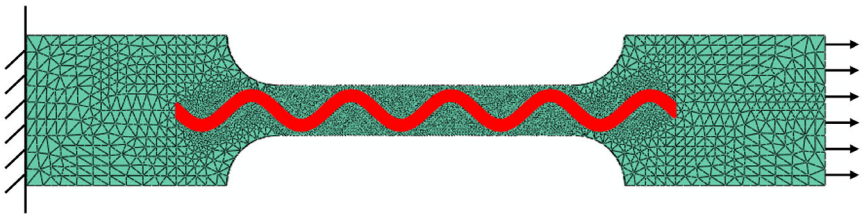

Figure 2. Meshed model of a laser-architectured sample.

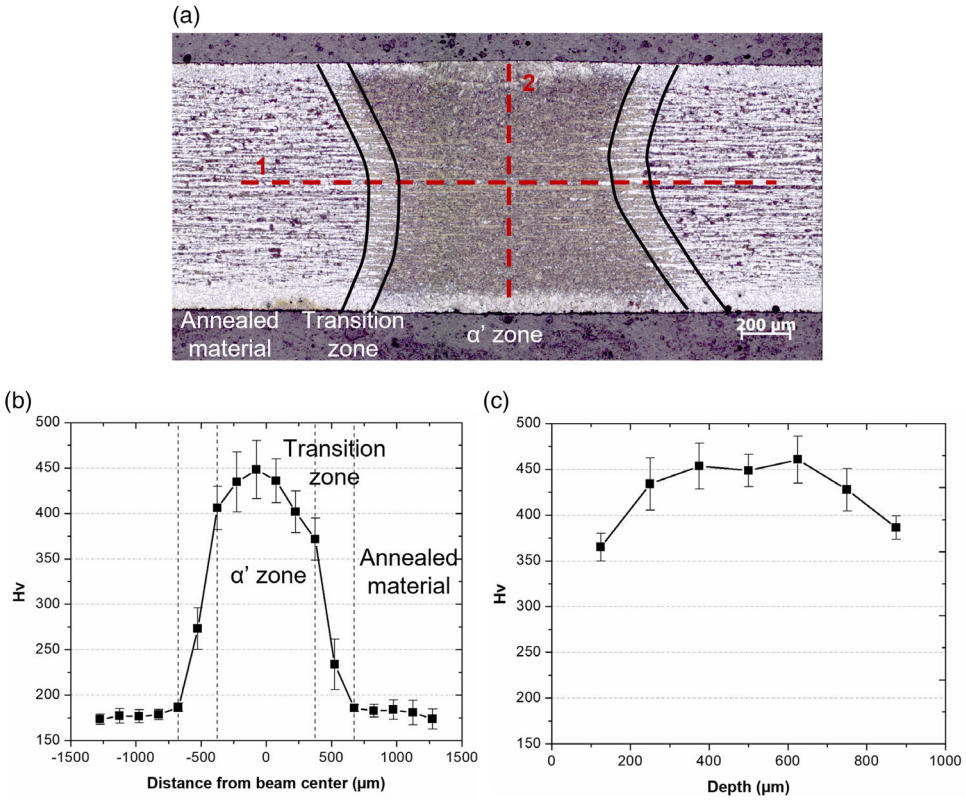

Figure 3. a) Microscopy of the laser-hardened zone, b) microhardness along the center line (track 1), and c) microhardness in the sheet along the beam center (track 2).

and lack of diffusion rate of carbon atoms, the austenization is not complete. The transition zone consists of graded martensite, which is formed where pearlite islands were previously embedded, that is., in ferrite grains (cf. Figure 4c). In Figure 4d, the peak temperature is above Ac3, both ferrite and pearlite transform into austenite so an almost fully martensitic zone is formed with only a small quantity of ferrite left. This graded microstructure results in the hardness gradient in Figure 3b and provides a clear contrast in strength between the matrix and reinforcement for the architectured material in this study.

3.2. Computational Approach

Finite-element method (FEM) simulations are performed on the sample geometries introduced in Table 2 in order to predict the tensile behavior of laser-architectured steel with straight or corrugated reinforcement. **Table 3** indicates the material parameters of matrix and reinforcement used in simulations. Beyond the yield strength (YS), plasticity of both matrix and reinforcement is assumed to follow the Hollomon strain hardening model in Equation (1), where K and n are respectively the hardening coefficient and strain hardening exponent. Matrix parameters are identified on the tensile test of annealed material and those of reinforcements are based on as-received martensitic steel. The behavior of both phases is assumed to be elastically and plastically isotropic.

$$\sigma = K\varepsilon^n \tag{1}$$

Figure 5a,b show the stress–strain curves of architectured steel samples with straight and corrugated reinforcements with fixed $P = 15$ mm and fixed $H = 1.5$ mm along with homogeneous

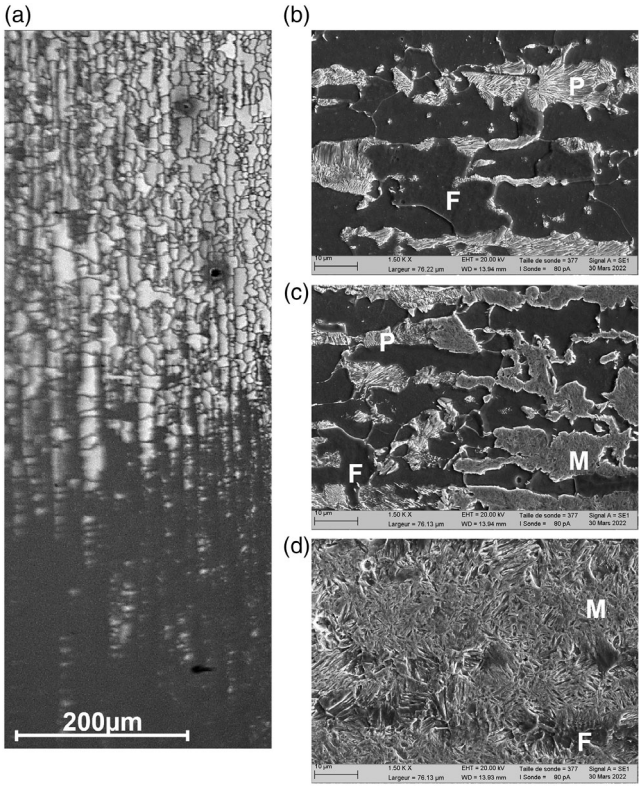

Figure 4. a) IQ of the cross section from annealed material to martensitic zone, microstructure of b) annealed material, c) transition zone, and d) martensitic zone.

Table 3. Material parameters used in FEM simulations.

	Matrix [ferrite + pearlite]	Reinforcement [martensite]
Young's modulus [GPa]	210	210
Poisson's ratio	0.3	0.3
YS [MPa]	280	1300
Strain hardening exponent [n]	0.24	0.06
Hardening coefficient *K* [MPa]	986	1966

matrix and reinforcement. All chosen patterns reinforce the soft matrix, increasing YS and ultimate tensile strength (UTS) and enhancing the necking strain compared to the stronger but brittle martensitic steel.

Focusing on heterogeneous reinforced samples, in Figure 5a, the straight reinforced sample has a poorest necking strain and an increase in corrugation height results in a gain in necking strain but a loss in YS and UTS. In Figure 5b, a smaller period also favors the necking strain and reduces YS and UTS. Figure 5c,d show the mechanical property evolutions according to the H/P ratio for both geometry strategies, that is, given period or given height. Even though the changes in the two cases do not follow the exact same linear relation, increasing the value of H/P has a similar trend to enhance the necking strain, which accompanies reduction in YS and UTS. The prediction of FEM simulation is to be verified by experiments in the following paragraphs.

3.3. Tensile Testing of Architectured Samples

Figure 6a,b shows the experimental tensile test results for samples with the reinforcement patterns given in Table 2 along with the mechanical response of pure ferritic matrix and pure martensitic reinforcement. Mechanical properties are summarized in **Table 4**. Homogeneous and heterogeneous samples have the same Young's modulus. All reinforcement geometries have a UTS above 750 MPa compared to 534 MPa of ferrite and a necking strain above 8% compared to 3.6% of martensite, which confirms the reinforcing effect of laser-induced architecture. The brittle reinforcement initiates the first crack with the strain increase and propagates to the matrix, which lead to the ultimate failure for all samples. No decohesion has taken place at the interface between the matrix and the reinforcement during the whole tensile tests, confirming that laser quenching generated an interface that is strong enough for architecturing steel, contrary to other architectured materials in which interfacial strength is commonly identified as a treat to mechanical performance and durability.

For each sample, the experimental YS and UTS are higher than corresponding numerical results. These discrepancies are caused by the hypothesis made in the FEM model of a perfect interface between matrix and reinforcement, without any transition zone. Nevertheless, while being relatively thin, the heat-affected zone between the laser-treated martensitic zone and ferritic matrix is observed experimentally (cf. Figure 3a), and this partly reinforced zone leads to higher strength compared to simulated results.

Despite this systematic gap between experimental and numerical results, similar trends are found while comparing results shown in Figure 6c,d with 5c,d. For a given period P (Samples 2, 3, 4), an increase corrugation height H leads to a gain in necking strain and a loss in YS and UTS. With the given corrugation height H (Samples 4, 5, 6), a reducing P gives the same trend. Comparing Sample 1 ($H/P = 0$) and Sample 6 ($H/P = 0.15$) as an example, the latter has a necking stain of 13.9%, while that of the former is only 8.3%, which corresponds to an increase of 67%, but at the same time the losses in YS and UTS are, respectively, 14% and 11%. Experimental results confirm the prediction of FEM simulation that an appropriate increase in the H/P ratio can enhance the necking strain with a trade-off in YS and UTS.

In order to understand the enhancing effect of corrugated reinforcements on necking strain, strain map evolutions on the gauge length are measured using DIC. **Figure 7** illustrates the local strain field evolutions, here with the principal strain component ε_{11} along the loading direction, of samples with different architecture patterns during the tensile test. As the matrix and reinforcement have the same Young's modulus, the elastic response is homogeneous for all samples. For Sample 1, with a straight reinforcement, the strain is always homogeneous in both the matrix and reinforcement all over the gauge length, as expected from composite theory, until strain localization gives rise to necking. For corrugation reinforced

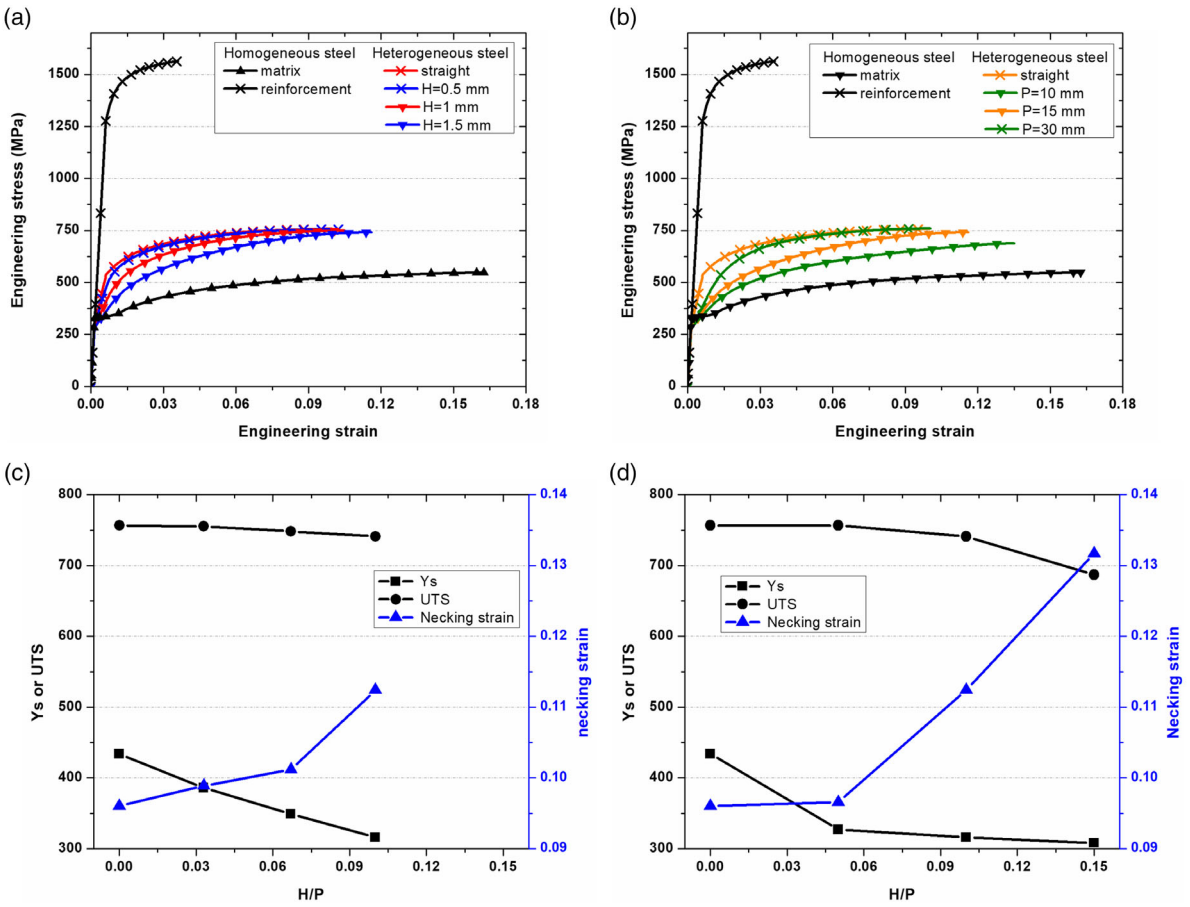

Figure 5. a) Numerical stress–strain curve of matrix, reinforcement, and samples with $P = 15$ mm and different heights, b) numerical stress–strain curve of matrix, reinforcement, and samples with $H = 1.5$ mm and different periods, and c,d) variations of YS, UTS, and necking strains of all samples in (a,b).

samples, the strain field becomes heterogeneous as plasticity starts. The local strain level in ferrite is much more important than that of martensite. It is noteworthy that specimens with corrugated reinforcements become wavy during tensile tests because of heterogeneous deformation, and the convex side is always opposite to the sinusoidal reinforcement.

Comparing Samples 2 and 4 at the same average total strain, it can be observed that an increase in corrugation height H for a given P results in a smaller strain level for martensite and larger for ferrite. The same influence on local strain can be found while comparing Samples 4 and 6 by reducing P with a given H. Corresponding FEM-simulated strain maps for an overall strain of 0.09 are shown in **Figure 8**, which depicts a local strain distribution similar to experimental DIC results. A higher inclination of the reinforced corrugation, that is, H/P ratio, leads to a localization of deformation in the matrix in place of the reinforcement. The higher the H/P ratio, the more heterogeneous the strain field. Because of the martensitic reinforcement being very brittle with an elongation of only around 4%, its fracture is always the first step of the specimen final failure. Therefore, a smaller local strain of the reinforcements due to a higher H/P can enhance the necking strain of the whole sample.

4. Discussion

4.1. Effect of Corrugated Reinforcement on Work Hardening

FEM simulation results indicate that corrugated reinforcements in architectured steel delay the necking strain compared to straight ones at the cost of a slight loss in YS and UTS. Experimental results shown in Figure 6 confirm this tradeoff. During tensile test, the work hardening rate of the reinforcement decreases rapidly to intersect the true stress while that of the matrix decreases much more slowly after the onset of plasticity, as shown in **Figure 9**a. This intersection corresponds to the necking start point defined by the Considère criterion.[47] Figure 9b,c shows that the intersections of work hardening rates and true stresses for architectured materials lie between matrix and reinforcement, and among them the straight reinforced sample has the lowest necking strain. For a given period (cf. Figure 9b), a larger height induces a smaller hardening rate, thus yielding a gain in necking strain. For a given height (cf. Figure 9c), a smaller period results in a similar effect. For both geometric parameters it can be concluded that a higher H/P ratio delays the intersection point of work hardening and true stress, that is, the onset of necking.

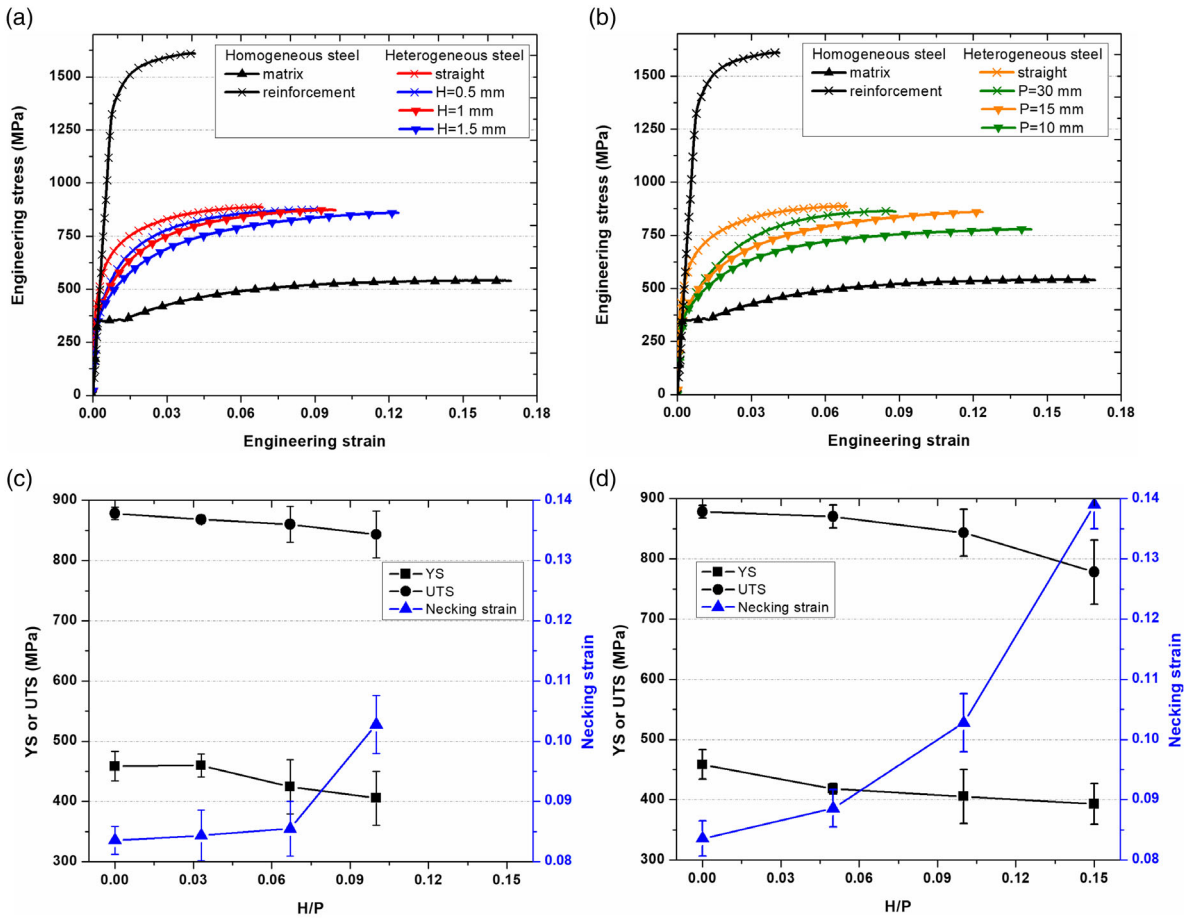

Figure 6. Experimental stress–strain curve of ferritic matrix and martensitic reinforcement with a) architectured samples with $P = 15$ mm and different heights, b) architectured samples with $h = 1.5$ mm and different periods, and c,d) variations of YS, UTS, and necking strain of all samples in (a,b).

Table 4. Mechanical properties of matrix, reinforcement, and architectured samples.

Sample	$[H]/P$	YS [MPa]	UTS [MPa]	Necking strain
Matrix	–	300 ± 7	534 ± 12	0.167 ± 0.003
Reinforcement	–	1388 ± 16	1553 ± 5	0.036 ± 0.001
1	0	458 ± 24	878 ± 10	0.083 ± 0.004
2	0.033	456 ± 19	868 ± 7	0.085 ± 0.004
3	0.067	424 ± 45	860 ± 30	0.086 ± 0.005
4	0.1	405 ± 44	843 ± 39	0.103 ± 0.005
5	0.05	418 ± 8	870 ± 18	0.089 ± 0.003
6	0.15	393 ± 33	778 ± 53	0.139 ± 0.004

This benefit on necking strain is due to the unbending process of the corrugation when loaded in tension. The configuration with corrugated reinforcement has a lower strength than straight reinforced configuration because the reinforcement is less aligned to the load direction.[40] During the uniaxial tensile test, the loading on fragments of corrugation can be divided into two perpendicular components: a component parallel to the fragment that accounts for its stretching and a perpendicular one responsible for unbending the fragment so that it becomes parallel with the longitudinal loading direction. The unbending process increases the strength of the whole sample with this change in reinforcement direction because the reinforcement is more and more aligned to the load direction. It increases the work hardening rate of the corrugated reinforcement and thus the global work hardening rate drop is delayed. This effect is due to the change in the geometry during the tensile test and thus the term called geometrically induced work hardening.[37]

With a higher H/P ratio, the initial reinforcement geometry is less aligned, and thus the YS is smaller. During the tensile loading, the increase in strength is more important, thus the geometrically induced work hardening becomes more visible. The work hardening rate drops more slowly and the intersection with true stress, where the necking is supposed to happen, is delayed. The parallel loading component in the reinforcement fragments is smaller and they are less deformed, which is the reason why a higher H/P ratio results in a more heterogeneous strain map at the same average total strain in Figure 7 and 8.

It is noteworthy that with the present laser-hardening method, and the matrix and reinforcement properties, the influence of material architecture on work hardening evolution during tensile

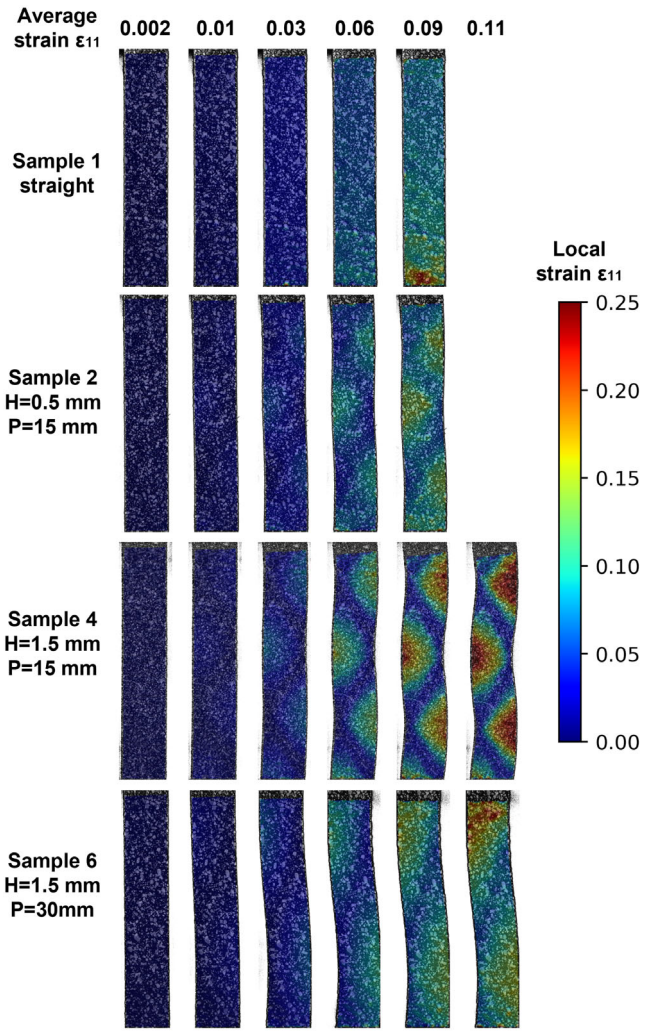

Figure 7. Strain field evolution during tensile tests on samples with different geometric patterns.

tests is limited to slowing down the drop in work hardening rate and delaying the onset of necking. With other combinations of matrix and reinforcement, it is possible to introduce a much more important effect on work hardening evolution thanks to the unbending process. The work of Fraser et al.[40] confirms with FEM simulation that an increase in work hardening rate may happen during tensile tests in a system of copper matrix and steel reinforcement. This inspiring result shows that a more obvious difference in strength between matrix and reinforcement may bring more obvious architecture effect, but likely at the cost of interfacial strength.

4.2. Perspective of the Corrugation Effect on Necking Strain

In this study, the chosen experimental geometrical parameters are limited in range for practical reasons, such as laser spot size, robot trajectory and moving velocity approximation, sample cutting precision, etc. But more geometries can be envisaged in order to exploit the corrugated reinforcement architecture effect if experimental conditions allow, for example, adjusting laser spot size or using an oscillation system. Some other parameters are tested by FEM simulation to estimate the reinforcement effect on mechanical properties, including reinforced volume fraction (from 12% to 48%), corrugation height (from 0.5 to 2 mm), and period (from 5 to 30 mm). **Figure 10**a,b summarizes the UTS and necking strain of samples with different geometric and volumetric reinforcements according to the H/P ratio with the chosen matrix reinforcement material system.

The UTS evolution of samples with various reinforced volume fractions follows a similar trend to previous results, as shown in Figure 10a. For a given H/P, UTS increases with an increasing reinforced volume fraction, and it decreases with the increasing H/P for a fixed reinforced volume fraction. The higher the reinforced volume fraction, the quicker the UTS drops with the growth of H/P. However, the necking strain evolutions of samples reinforced with different volume fractions do not

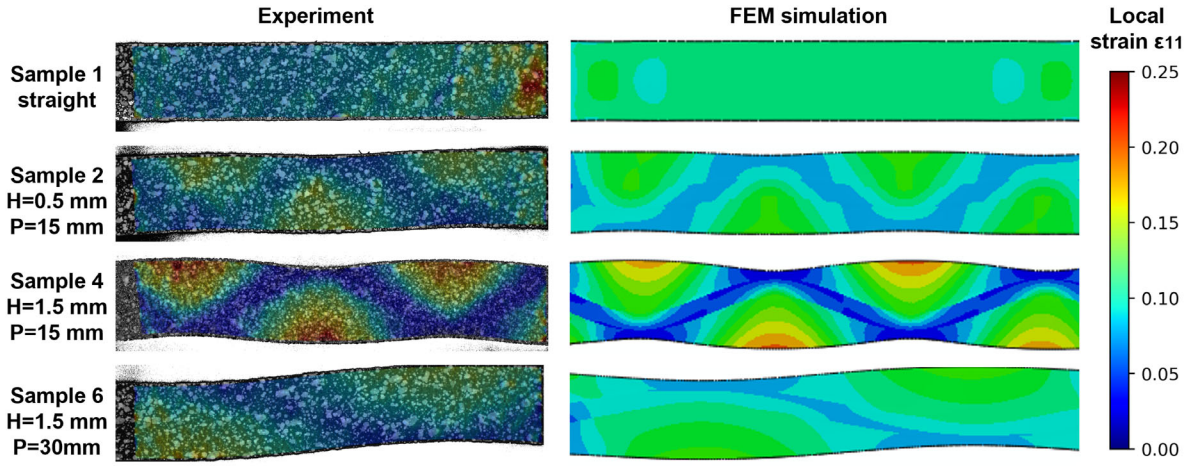

Figure 8. Experimental and FEM simulation strain maps of architectured samples at a total strain of 0.09.

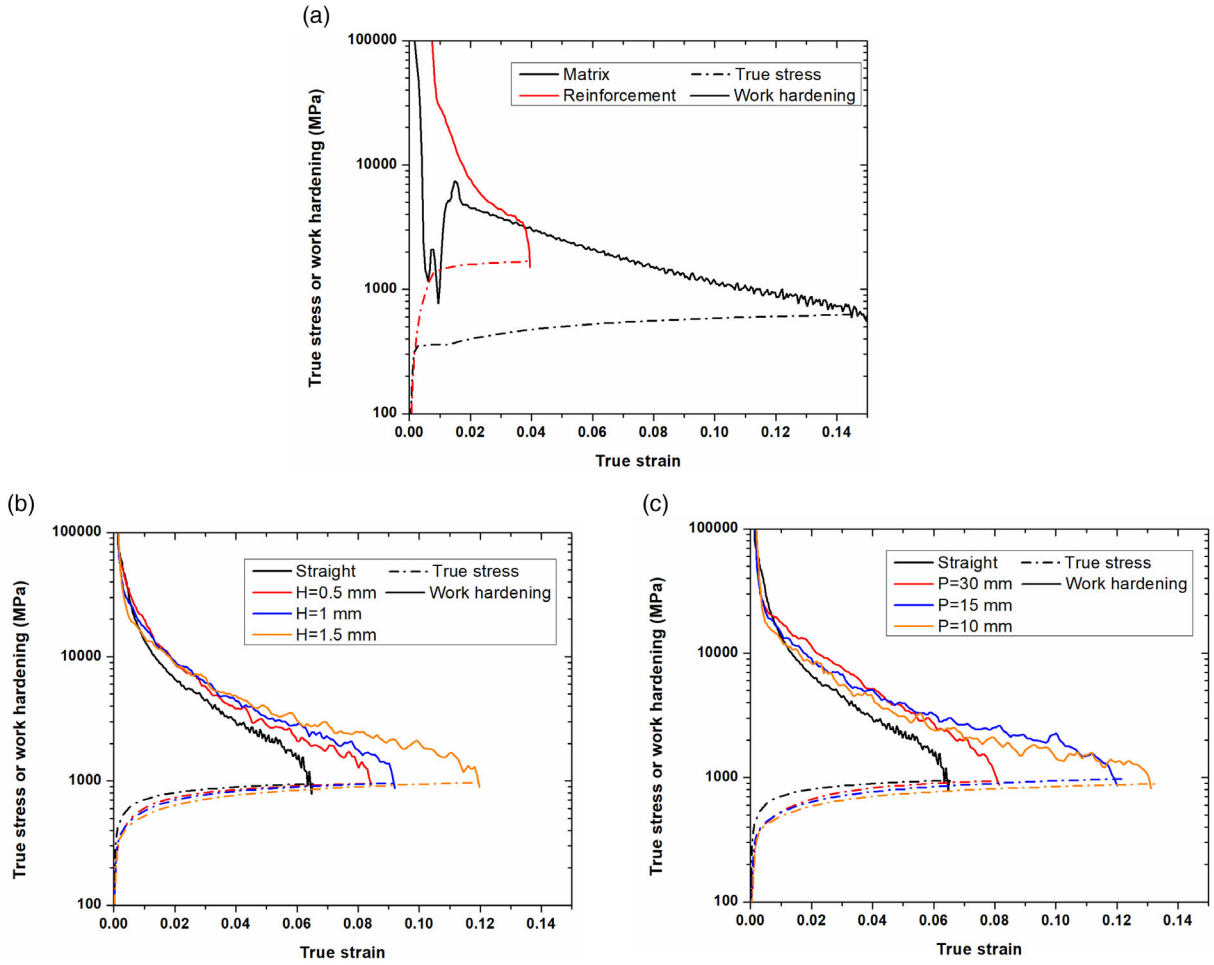

Figure 9. True stress and work hardening behavior of a) matrix and reinforcement, b) architectured steel with straight and corrugated reinforcement of $P = 15$ mm, and c) architectured steel with straight and corrugated reinforcement of $H = 1.5$ mm.

present the same trend as before in Figure 10b. With 12% reinforcement, the necking strain decreases at the beginning with H/P below 0.1 and it starts to increase slightly with H/P between 0.1 and 0.2. With 24% reinforcement, the benefit effect on necking strain is negligible for H/P below 0.067 before increasing. But with 36% and 48% of reinforced volume fraction, the gain in necking strain is visible immediately with an increasing H/P until 0.2. Beyond this value, the gain in necking strain for all samples vanishes, or becomes negative even. Thus, for a certain reinforced volume fraction, a threshold inclination ratio H/P is required in order to achieve an architecture-induced benefit on necking strain. This threshold value is lower when the reinforced volume fraction is higher. As the martensitic phase is very hard and brittle, increasing the volume fraction increases the strength of architectured samples but reduces the necking strain. It can be inferred that all fracture events initiate from the martensitic reinforcement and propagate into the matrix.

Figure 10c shows the UTS necking strain relation of all geometries along with homogeneous matrix and reinforcement. The UTS and necking strain of architectured samples are always between those of the matrix and reinforcement. With the change in geometric parameters and reinforcement volume fractions, samples are located in different regions in this property map. The upper right zone is the target to resolve the contradiction between the ductility and strength of advanced high-strength steel, which is hard to access for homogeneous steel by the traditional metallurgical method. Corrugated architectured steel may provide a potential way to fill gaps in the material–property space. Figure 10d summarizes the plastically dissipated energy of all studied geometries with their H/P, which presents a similar trend with the necking strain. With 12% volume reinforced, the absorbed energy decreases with the increasing of H/P. But with more reinforced volume fraction, it increases until H/P is around 0.1 and then decreases due to settled necking strain and reduced UTS. Together with UTS and necking strain, plastically dissipated energy can also be a criterion to evaluate architectured material mechanical properties.

While most of the samples probed using FEM have an intermediate plastically dissipated energy, between those of the pure homogeneous matrix and reinforcement, several architectures generate a higher dissipated energy value than that of the matrix in Figure 10d. These configurations correspond to specimens

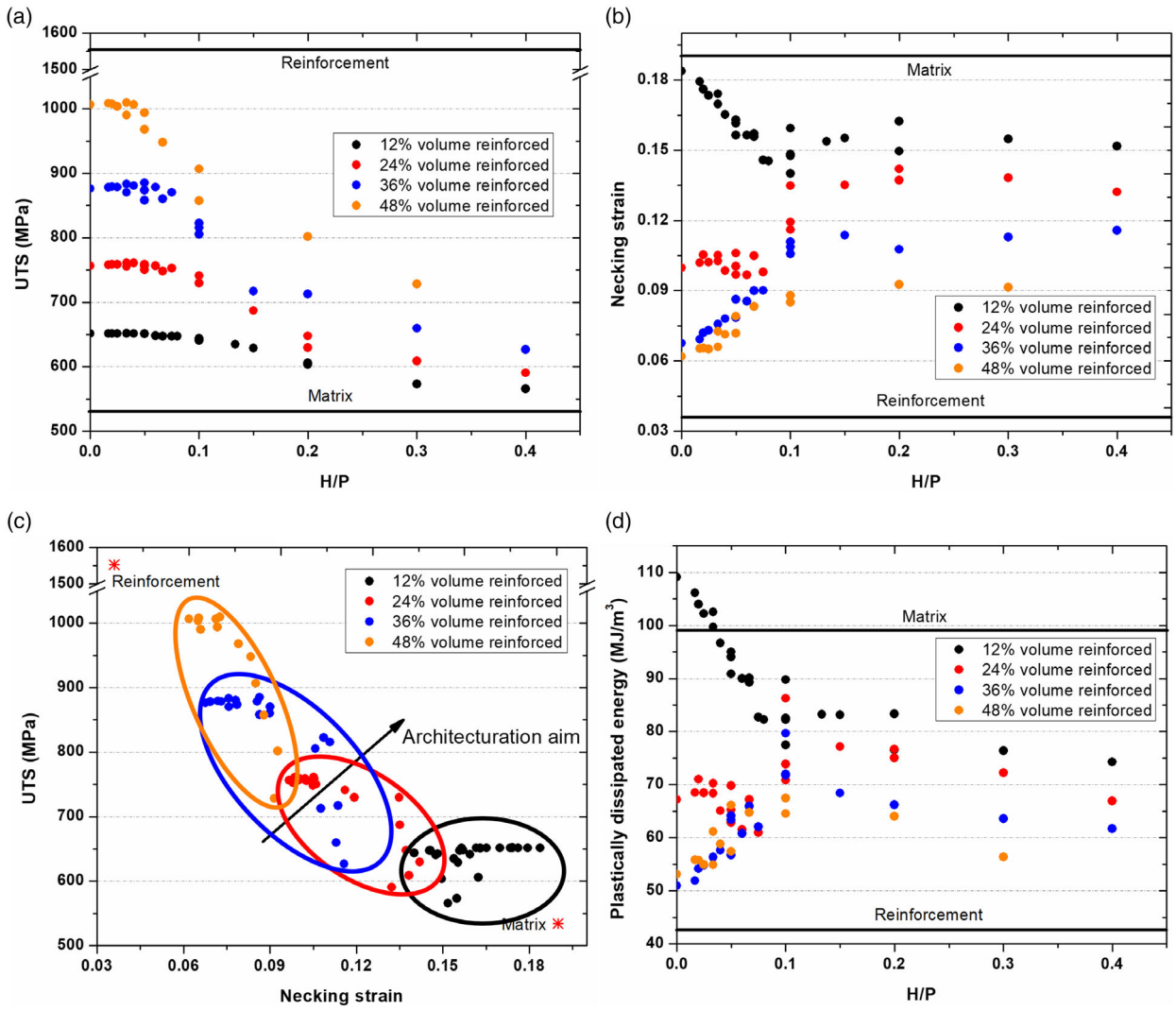

Figure 10. FEM simulation results: a) UTS evolution with H/P, b) necking strain evolution with H/P, c) UTS–necking strain relationship, and d) plastically dissipated energy evolution with H/P.

with 12% of reinforced volume and a small corrugation inclination, with H/P below 0.03. Together with the positions of these configurations in Figure 10a,b, this superior dissipated energy comes from a remarkable increase in strength, of about 120 MPa, and relatively low ductility loss, about 2%, compared to ferrite. Beyond this H/P value and reinforced volume fraction, the gain in strength cannot compensate the loss in ductility, thus yielding a lower value for plastically dissipated energy. Therefore, Figure 10 gathers several design maps enabling the possibility of choosing the suitable architecture for specific requirements in terms of mechanical properties, including architectures that outperform their constitutive phases.

Finally, this processing strategy for laser-induced architectures should be applicable to other laser-hardenable metallic materials, such as Al and Ti alloys,[48,49] but alternative architecture patterns as well as laser treatments, such as laser alloying, laser softening, or laser shock peening, could also be considered for future research.

5. Conclusion

1) With suitable parameters, local laser treatment can harden the ferritic matrix efficiently, thanks to rapid cooling. The hardness of the treated zone is around 430 Hv compared to 174 Hv of the annealed steel and the whole thickness presents rather stable hardness. This obvious contrast can provide a soft but ductile matrix and a hard but brittle reinforcement. 2) Localized laser quenching of ferritic steel generates a strong, diffuse, although limited in the thickness, interfacial zone, which mitigates decohesion, therefore avoiding a failure mode commonly observed in architectured materials. 3) Two geometric corrugation strategies, fixed height with varying periods and fixed period with varying heights, confirm both that an increase in corrugation inclination ratio H/P improves necking strain but reduces YS and UTS. This beneficial effect on necking strain is due to work hardening boost induced by the unbending process of the corrugated reinforcements. 4) Extended simulation prediction on the larger

parametric range shows that the UTS and necking strain depend on the corrugation inclination H/P. A threshold for H/P is needed to improve the necking strain for samples with smaller reinforced volume fraction. 5) Computational analysis yielded architectures that outperform both pure ferrite and pure martensite in terms of plastically dissipated energy. Corrugated reinforcement as an architectured material strategy has the potential to fill gaps in the material–property space, by improving the strength-to-ductility tradeoff.

Acknowledgements

This work was funded by Agence Nationale de la Recherche through the ANR JCJC SCOLASTIC (Systematic Computational Optimization and Local Laser Processing for Steel-Based Architectured Materials) project (grant number 16-CE08-0009).

Conflict of Interest

The authors declare no conflict of interest.

Data Availability Statement

The data that support the findings of this study are available from the corresponding author upon reasonable request.

Keywords

architectured materials, corrugated materials, laser processing, mechanical properties, steels

Received: September 9, 2022
Revised: January 1, 2023
Published online:

[1] M. F. Ashby, Y. Bréchet, *Acta Mater.* **2003**, *51*, 5801.
[2] M. F. Ashby, *Scr. Mater.* **2013**, *68*, 4.
[3] O. Bouaziz, Y. Bréchet, J. D. Embury, *Adv. Eng. Mater.* **2008**, *10*, 24.
[4] Y. Zhu, K. Ameyama, P. M. Anderson, I. J. Beyerlein, H. Gao, H. S. Kim, E. Lavernia, S. Mathaudhu, H. Mughrabi, R. O. Ritchie, N. Tsuji, X. Zhang, X. Wu, *Mater. Res. Lett.* **2021**, *9*, 1.
[5] O. Bouaziz, *Scr. Mater.* **2013**, *68*, 28.
[6] Y. Bréchet, J. D. Embury, *Scr. Mater.* **2013**, *68*, 1.
[7] V. S. Deshpande, M. F. Ashby, N. A. Fleck, *Acta Mater.* **2001**, *49*, 1035.
[8] G. W. Kooistra, V. S. Deshpande, H. N. Wadley, *Acta Mater.* **2004**, *52*, 4229.
[9] N. A. Fleck, V. S. Deshpande, M. F. Ashby, *Proc. Roy. Soc. A: Math. Phys. Eng. Sci.* **2010**, *466*, 2495.
[10] T. A. Schaedler, A. J. Jacobsen, A. Torrents, A. E. Sorensen, J. Lian, J. R. Greer, L. Valdevit, W. B. Carter, *Science* **2011**, *334*, 962.
[11] T. Tancogne-Dejean, A. B. Spierings, D. Mohr, *Acta Mater.* **2016**, *116*, 14.
[12] R. M. Latture, R. X. Rodriguez, L. R. Holmes Jr., F. W. Zok, *Acta Mater.* **2018**, *149*, 78.
[13] A.-E. Viard, J. Dirrenberger, S. Forest, *Int. J. Solids Struct.* **2020**, *202*, 532.
[14] R. S. Lakes, *Science* **1987**, *235*, 1038.
[15] G. W. Milton, *J. Mech. Phys. Solids* **1992**, *40*, 1105.
[16] F. Scarpa, J. R. Yates, L. G. Ciffo, S. Patsias, *Proc. Inst. Mech. Eng. C J. Mech. Eng. Sci.* **2002**, *216*, 1153.
[17] A. Alderson, K. L. Alderson, D. Attard, K. E. Evans, R. Gatt, J. N. Grima, W. Miller, N. Ravirala, C. W. Smith, K. Zied, *Compos. Sci. Technol.* **2010**, *70*, 1042.
[18] M. Bianchi, F. Scarpa, M. Banse, C. W. Smith, *Acta Mater.* **2011**, *59*, 686.
[19] C. Körner, Y. Liebold-Ribeiro, *Smart Mater. Struct.* **2015**, *24*, 025013.
[20] C. Soyarslan, V. Blümer, S. Bargmann, *Acta Mater.* **2019**, *177*, 280.
[21] A. V. Dyskin, Y. Estrin, A. J. Kanel-Belov, E. Pasternak, *Adv. Eng. Mater.* **2001**, *3*, 885.
[22] Y. Estrin, A. V. Dyskin, E. Pasternak, *Mater. Sci. Eng.* **2011**, *C31*, 1189.
[23] A. Molotnikov, R. Gerbrand, Y. Qi, G. P. Simon, Y. Estrin, *Smart Mater. Struct.* **2015**, *24*, 025034.
[24] L. Djumas, G. P. Simon, Y. Estrin, A. Molotnikov, *Sci. Rep.* **2017**, *7*, 11844.
[25] M. Mirkhalaf, T. Zhou, F. Barthelat, *PNAS* **2018**, *115*, 9128.
[26] S. Suresh, A. E. Giannakopoulos, J. Alcalá, *Acta Mater.* **1997**, *45*, 1307.
[27] J.-C. Han, B.-L. Wang, *Acta Mater.* **2006**, *54*, 963.
[28] B. Chéhab, H. Zurob, D. Embury, O. Bouaziz, Y. Bréchet, *Adv. Eng. Mater.* **2009**, *11*, 992.
[29] R. Cicoria, B. Chehab, H. Zurob, *Scr. Mater.* **2013**, *68*, 17.
[30] H. Naser, A. Deschamps, M. Mantel, M. Véron, *Mater. Des.* **2018**, *145*, 156.
[31] H. Azizi, H. S. Zurob, D. Embury, X. Wang, K. Wang, B. Bose, *Acta Mater.* **2018**, *143*, 298.
[32] H. Azizi, X. Wang, D. Embury, H. S. Zurob, *Materialia* **2020**, *13*, 100831.
[33] H. Azizi, J. Samei, H. S. Zurob, D. S. Wilkinson, D. Embury, *Mater. Sci. Eng. A* **2022**, *833*, 142582.
[34] O. Bouaziz, S. Allain, D. Barcelo, R. Niang, *MRS Proc.* **2009**, *1188*, 1188-LL05-01.
[35] M. Delincé, Y. Bréchet, J. D. Embury, M. G. D. Geers, P. J. Jacques, T. Pardoen, *Acta Mater.* **2007**, *55*, 2337.
[36] A. P. Pierman, O. Bouaziz, T. Pardoen, P. J. Jacques, L. Brassart, *Acta Mater.* **2014**, *73*, 298.
[37] O. Bouaziz, S. Allain, C. Scott, *Scr. Mater.* **2008**, *58*, 484.
[38] C. Thill, J. A. Etches, I. P. Bond, K. D. Potter, P. M. Weaver, M. R. Wisnom, *Compos. Part A Appl. Sci. Manuf.* **2010**, *41*, 168.
[39] I. Dayyani, S. Ziaei-Rad, H. Salehi, *Appl. Compos. Mater.* **2012**, *19*, 705.
[40] M. Fraser, H. S. Zurob, P. Wu, *Adv. Eng. Mater.* **2018**, *20*, 1700834.
[41] M. Fraser, H. Zurob, P. Wu, O. Bouaziz, *Materials* **2020**, *13*, 5175.
[42] J. Ion, in *Laser Processing Of Engineering Materials*, Elsevier, Oxford **2005**.
[43] E. Capello, B. Previtali, *J. Laser Appl.* **2009**, *21*, 1.
[44] P. Lapouge, J. Dirrenberger, F. Coste, M. Schneider, *Mater. Sci. Eng. A* **2019**, *752*, 128.
[45] Z. Wang, J. Dirrenberger, P. Lapouge, S. Dubent, *Mater. Sci. Eng. A* **2022**, *831*, 142205.
[46] Z. Wang, J. Dirrenberger, P. Lapouge, S. Dubent, H. Jabir, V. Michel, *J. Eng. Mater. Technol.* **2022**, *144*, 041005.
[47] A. Considère, *Ann. des Ponts et Chaussées* **1885**, *1*, 574.
[48] P. Chandrasekar, V. Balusamy, K. S. R. Chandran, H. Kumar, *Scr. Mater.* **2007**, *56*, 641.
[49] N. Takata, M. Liu, H. Kodaira, A. Suzuki, M. Kobashi, *Addit. Manuf.* **2020**, *33*, 101152.